Solution of Singularities in Boundary Methods for Fluid dynamics using Node Displacement and Analytic Integral Evaluation.

Samuel Velez-Sanin[1] Cristian Rendon-Cardona[1]
Juan Diego-Jaramillo[2] Nicolas Guarín-Zapata[2]
Oscar Ruiz-Salguero[1]

[1] CAD CAM CAE Laboratory - Universidad EAFIT, Colombia
[2] Grupo de Mecánica Aplicada - Universidad EAFIT, Colombia

May 14, 2022

Abstract

In the domain of Boundary Element Methods, computing the effect of a loaded node upon itself entails the solution of singular integrals (boundary and surface). These singular integrals introduce discontinuities in the Boundary Integral Equation. For Steady Incompressible Viscous Flow, existing solutions for these integrals are (a) sub-segmentations of the integration domain, (b) integration over a lumped non-singular domain. Strategy (a) produce high computing expenses. Strategy (b) implies increased integration complexity. In facing these limitations, this manuscript presents an implementation of the source-node displacement method to compute the singular boundary integrals. We then use a direct analytic integration for the singular surface integrals. To our knowledge, these methods have not been previously used for Fluid Dynamics problems. Our implementation approximates the boundary and surface singular integrals.

The numerical examples computed with these integral results predict laminar flow around submerged objects. Some differences in the velocity field between simulations (BEM-ANSYS) are encountered. In addition, other numerical examples present divergence of the boundary results. These problems may occur due to unaccounted factors such as incorrect discretization of the problem domain or incorrect definition of boundary conditions. Even though, the singular integrals can be approximated by the means presented and used for simulations.

Glossary

este es el glosario

Ω	Boundary value problem's 2-dimensional domain that contains part of its border. Domain of the velocity vector field. May be unbounded or bounded.
B	Subset of the boundary (border) of Ω. $B \subset \Omega$. Scenario for the boundary singular integrals. Thus, it is the focus of our contribution.
Γ_0	External LOOP of B in case Ω being bounded.
Γ_i	Internal LOOP of B.
R	Interior of Ω. $R = int(\Omega)$ with $int(\Omega) = \Omega - B$.
S	$S \subset R$. Region in which the non-linear convective acceleration effects are significant.
x_i	[m] i-th component of a the Cartesian coordinate of a point $\in \Omega$. $i = 1, 2$.
u_i	[m] i-th component of an absolute velocity vector. $i = 1, 2$.
v_i	[m] i-th component of a velocity perturbation vector. $i = 1, 2$.
V_i	[m] i-th component of the free flow velocity vector. $i = 1, 2$.
f_i	$[\frac{\mathrm{N}}{\mathrm{m}^2}]$ i-th component of a traction vector. $i = 1, 2$.
$\vec{f}_i$	[N] i-th component of a body force vector. $i = 1, 2$.
ρ	$[\frac{\mathrm{kg}}{\mathrm{m}^3}]$ Fluid's density (assumed constant for this manuscript).
μ	$[\frac{\mathrm{Ns}}{\mathrm{m}^2}]$ Fluid's dynamic viscosity (assumed constant for this manuscript).
X	[m,m] Field element position vector.
ξ	[m,m] Source element position vector.

AIG	Analytic integration (source node displacement method) result of the Green function G in the canonical coordinate system.
${}^{o}AIG$	Analytic integration (source node displacement method) result of the Green function in the $x\,y$ cartesian coordinate system.
M	Total number of boundary elements.
L	Total number of interior elements.
m	Identifier of a boundary element.
l	Identifier of an interior element identifier.
$\hat{n}$	Unitary normal vector of a boundary element.
r	$[m, m]$ Position vector of field element X w.r.t source element ξ.
δ	[ ] Kronecker's delta.
$\mathbf{t}$	1-dimensional array whose entries are the values of the components $(i = 1, 2)$ of the traction vector at boundary elements.
$\mathbf{v}$	1-dimensional array whose entries are the values of the components $(i = 1, 2)$ of the velocity perturbation vector at boundary elements.
$\mathbf{t^o}$	1-dimensional array whose entries are the values of the components $(i = 1, 2)$ of the convective traction vector at boundary elements.
$\sigma^{\mathbf{o}}$	1-dimensional array whose entries are the values of the components $(i = 1, 2)$ of the convective traction tensor at interior elements.
$\mathbf{G}$	Rectangular matrix whose entries are the results of the boundary integrals of Green function G_{ij} for each r.

F	Rectangular matrix whose entries are the results of the boundary integrals of Green function F_{ij} for each r.
D	Rectangular matrix whose entries are the results of the surface integrals of Green function $\frac{\partial G_{ij}}{\partial x_k}$ for each r.
Convective acceleration	$[\frac{\mathrm{m}}{\mathrm{sm}}]$ Change of speed produced by changes in spatial position. $\frac{\partial u_i}{\partial x_j}$
Ω_r	Mesh triangular element.
Ω_c	Canonical triangular element.

1 Introduction

In the Boundary Element Method (BEM) formulation, the evaluation of Green functions existent in the Boundary Integral Equation (BIE) presents divisions by 0 and ln(0) (singularities). These singularities occur when evaluating the effects on element/node j due to a load applied on element/node i, when $i = j$. Since these singular integrals are fundamental to BEM, this manuscript presents two methods for avoiding/solving the boundary and interior singular integrals for steady incompressible viscous flow, and constant (order 0) elements.

Roughly speaking, the implemented method for the boundary singular integrals is as follows. (1) A displacement $\Delta = (0, D)$ is introduced to node i of a canonical element. (2) We define and evaluate the integrals in the analytic domain. (3) The $\lim D \to 0$ is taken for the symbolic results. (4) The results are transformed for the real elements. This method was first introduced for the fracture and elasticity fields, we are extending it to fluid dynamics.

For the interior singular integrals, despite the fact that the Green function is singular, the integrals are finite and their results exist. Therefore, an analytic evaluation of the integrals, without avoiding the singularity, is performed over a canonical 2-D triangular cell and the result is then transformed for the real element.

We tested the method for the boundary integrals by steps 1-3. Since there were no results found in the literature for the interior singular integrals and the fact that they were already evaluated analytically, the results were only tested by step 3.

We compared the results for the canonical element to solutions found in literature computed with different methods.

1. For 6/8 of the boundary integrals, our solution and the published solutions are the same.

2. For the 2/8 integrals that did not yield the same result, we evaluated the analytic integral without avoiding the singularity. The results were identical to the ones computed by our solution. It must be mentioned that, even though these particular integrals can be computed without avoiding the singularity, it isn't the case for the other integrals and the method presented is necessary.

3. We computed Fluid Dynamics scenarios with our BEM scheme (handling the singular cases) and compared them qualitatively to the same scenarios computed with ANSYS. We obtain similar results with some differences that can be explained by factors such as discretization and fundamental differences between the two simulation methods.

For these reasons, we consider that this manuscript contributes to the available tools that BEM practitioners have at their disposal, and opens opportunities for handling the aforementioned singularities in higher degree elements and other fields.

1.1 Problem Specification

We define the Boundary Element Problem (BEP) as the continuous formulation of BEM, which includes the continuous BIE and the definition of a continuous domain, for solving a partial differential equation (PDE). For this manuscript, the PDE is the Navier-stokes equation for 2-dimensional Steady Incompressible Viscous flow. Since a solution for BEP is difficult to obtain and not treated in literature, a piece-wise linear approximation ($\widetilde{BEP}$) is considered. The fact that $\widetilde{BEP}$ approximates or not the solution of BEP is a fundamental discussion of Boundary Element Methods (BEM). As a consequence, this document does not treat this aspect but focuses on the solution of the singular integrals (for constant -order 0- boundary and interior elements) found in $\widetilde{BEP}$. Which are needed to obtain an approximate solution for BEP by solving $\widetilde{BEP}$.

This manuscript is organized as follows: Section 2 discusses the relevant literature. Section 3 presents the approximation of the BEP and the proposed method to avoid the singularities in the Boundary/Surface integrals of $\widetilde{BEP}$. Section 4 discusses the results of various simulations. Finally, section 5 discuses the conclusions and introduces to future work.

2 Literature Review

The current literature for avoiding the singularities present in general BEM formulations is divided into three main categories. (1) Sub-segmentations of the integration domain, (2) distortion of the singular boundary/surface element, (3) displacement of the source node in the boundary/surface element. Table 2 presents the main advantages and disadvantages of these main categories.

2.1 Element Sub-segmentation

The integration domain (singular element) is subdivided into smaller domains around the singular position. A numerical integration (quadrature scheme) is computed in the resulting non-singular domains. Depending on the type of singularity, special quadrature schemes may be utilized for the remaining singular part. In some cases, the singular part is computed in the Cauchy Principle Value sense. Refs. [6, 9, 11, 13, 17, 21, 20] present their methods in the fields of elasticity, fluid dynamics and elastodynamics.

2.2 Distortion of the Singular Element

The singular element is distorted (lumped) in order to separate the boundary from the source node. In consequence, the previous singular kernels can be integrated analytically with a coordinate transformation and then the limit is computed for shrinking the boundary to its original state. Ref. [1] presents their method in the field of Fluid Dynamics, Ref. [10] for a general case, and Ref. [18] implements the method in the field of elasticity.

2.3 Displacement of the Source Node

The source node is displaced from the singular element (boundary). Consequently, the integrand (Green function) is modified, becoming non-singular and the integral is evaluated analytically. Finally, the limit is taken as the source node approaches the boundary to obtain the singular integral result. Refs. [2, 12] present their method in the fields of elasticity and fracture analysis, respectively.

2.4 Conclusions of Literature Review

Table 2: Different approaches and our contribution.

Approach	**Refs.**	**Advantages**	**Disadvantages**
Sub-segmentation of the singular boundary/surface element	[6, 8, 9, 11, 13, 17, 20, 21]	(1) Possible errors present in complex analytic/symbolic evaluation of integrals are avoided. (2) Element order scalability.	(1) High computational cost for the evaluation of each segment. (2) Complex quadrature schemes are needed for singular or near-singular integrals. (3) Prone to quadrature errors.
Distortion of the singular boundary/surface element	[1, 10, 15, 18]	(1) Simple computation of integrals with pre-calculated formulae.	(1) Increased complexity of the integration scheme because of domain coordinate transformations.
Displacement of the source node in the singular canonical boundary/surface element (our approach)	[2, 12]	(1) Simple computation of integrals with pre-calculated formulae. (2) No modification of the integration domain, no need for coordinate transformation.	(1) Complex analytic integration, prone to errors.

To the best of our knowledge, for the specific fluid dynamics field mentioned in Section 1, the only implemented methods to compute the singular integrals are the sub-segmentation and distortion methods (Refs. [1, 6, 8]). The displacement of the source node method has not yet been implemented and tested. As a consequence, this manuscript implements it as an alternative to compute the boundary singular integrals of the Green functions present in the BEM formulation for the specific flow. In addition, a direct analytic evaluation of the surface singular is presented since, which to the best of our knowledge, has not been utilized in the specific flow. These methods present the advantage of allowing for low computational costs and no integration domain mapping, which permits a simpler implementation and it is less prone to analytic integration errors.

3 Methodology

3.1 Assumptions and Preconditions

The Boundary Element Method formulation presented in this section is strongly based on the formulation proposed by [8] for Steady Incompressible Thermoviscous flow. It is our simplification for the flow characteristics specified in section 1 and numerical treatment of BEM. The simplifications are (1) The flow is adiabatic and isotherm leading to a simplified system of governing equations, (2) Green functions presented by [8] also represent the flow of this manuscript, (3) low order elements (constant) are used for the discretization of the boundary (B) and surface (S), (4) the singular integrals (B and S) are approached in an analytic way (scenario of our contribution), (5) near singular cases are not taken into account.

3.2 Domain Layout

The general domain layout for this manuscript is presented on Figure 1. Complete domain $\Omega = R \cup B$, with B being the boundary and R the interior region. The boundary B is conformed by $\Gamma_0 \cup \Gamma_i$, the exterior and interior boundaries, respectively.

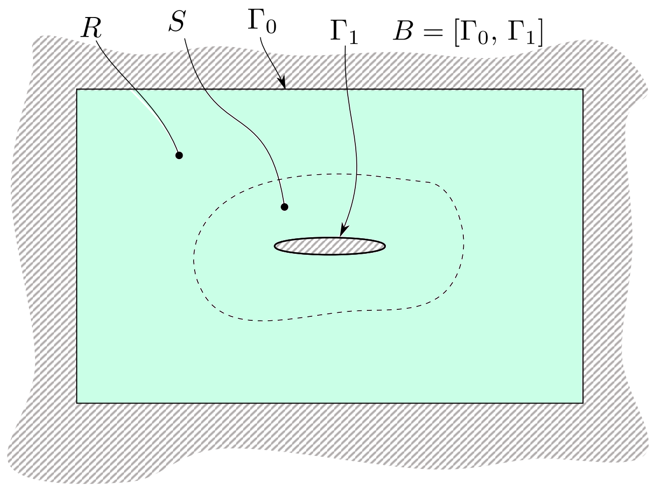

Figure 1: BEP domain layout. $\Omega = R \cup B$.

3.3 Governing Equations

The governing equations for Steady Incompressible Thermoviscous Flow presented in [8] are as follows , were summation convention is used:

$$\text{Mass conservation:} \quad \frac{\partial u_j}{\partial x_j} = 0. \tag{1}$$

$$\text{Momentum conservation:} \quad \mu \frac{\partial^2 u_i}{\partial x_j \partial x_j} - \frac{\partial p}{\partial x_i} - \rho u_j \frac{\partial u_i}{\partial x_j} + \vec{f}_i = 0. \tag{2}$$

$$\text{Energy conservation:} \quad k \frac{\partial^2 \theta}{\partial x_j \partial x_j} - \rho c_\varepsilon u_j \frac{\partial \theta}{\partial x_j} + \Upsilon + \Psi = 0. \tag{3}$$

For purposes of this work, some assumptions are introduced to Eqs. (1-3). These are:

1. Constant temperature,

$$\frac{\partial \theta}{\partial x_i} = 0.$$

2. Heat sources and viscous dissipation are not considered,

$$\Upsilon = 0, \quad \Psi = 0.$$

Because of statements 1 and 2, Eq. (3) is not considered.

3. There aren't any body forces,

$$\vec{f_i} = 0.$$

After applying the assumptions, the resulting governing equations are:

$$\text{Mass conservation:} \quad \frac{\partial u_j}{\partial x_j} = 0. \tag{4}$$

$$\text{Momentum conservation:} \quad \mu \frac{\partial^2 u_i}{\partial x_j \partial x_j} - \frac{\partial p}{\partial x_i} - \rho u_j \frac{\partial u_i}{\partial x_j} = 0. \tag{5}$$

3.4 Continuous Formulation of the BEM Integral Equation

With all the assumptions presented in section 3.3 and the linearization of the non-linear convective term assumed by [8], the Eq. (16a) from [8] is rewritten in Eq. (6). This is the continuous integral formulation of the Boundary Element Method to be solved. Because of the linearization, the boundary solution has to be iterated to obtain convergence. This is discussed later in the manuscript.

The formulation of the BEM equation is presented in terms of v_i (velocity perturbation) and t_i (traction) instead of u_i (absolute velocity) and p (pressure) as in Eq. 5. Such change of variables and formulation corresponds to the presented by [8]. It is not detailed in this manuscript since it does not correspond to the focus of the present work. Some of the terms of Eq. 6 are described in Table 3. See also [1] for a detailed development of the boundary integral equation in terms of velocity and traction.

$$
\begin{aligned}
c_{ij}(\xi)v_i(\xi) = &\int_B [G_{ij}(X-\xi)t_i(X) - F_{ij}(X-\xi)v_i(X) \\
&-G_{ij}(X-\xi)\rho(V_k(X)+v_k(X))n_k(X)v_i(X)]dB(X) \\
&-\int_S \left[\frac{\partial G_{ij}(X-\xi)}{\partial x_k}\rho(V_k(X)+v_k(X))v_i(X)\right] dS(X).
\end{aligned} \tag{6}
$$

Table 3: Terms description for the continuous BEM equation. T: Time units, L: Distance units, M: Mass units.

Term	**Description**	**Dims.**
V_i.	Free flow velocity vector.	$\frac{L}{T}$.
$v_i = u_i - V_i$.	Velocity perturbation vector.	$\frac{L}{T}$
t_i.	Traction vector.	$\frac{M}{LT^2}$
$c_{ij}(\xi) = \delta_{ij}/2$.	Constant term.	-

3.4.1 Green Functions

Eqs. (7 - 9) present the Green Functions utilized in Eq. (6). Singularities occur when $X_i = \xi_i$, making $r^2 = 0$. F_{ij} is assumed positive (as in [1]) for purposes of this work.

$$G_{ij} = \frac{1}{4\pi\mu}\left(\frac{y_i y_j}{r^2} - \delta_{ij}\ln r\right). \tag{7}$$

$$F_{ij} = \frac{1}{2\pi r}\left(\frac{2y_i y_j y_k n_k}{r^3}\right). \tag{8}$$

$$\frac{\partial G_{ij}}{\partial x_k} = \frac{1}{4\pi\mu r}\left(\frac{\delta_{jk}y_i}{r} + \frac{\delta_{ik}y_j}{r} - \frac{\delta_{ij}y_k}{r} - \frac{2y_i y_j y_k}{r^3}\right). \tag{9}$$

$$y_i = X_i - \xi_i. \tag{10}$$

$$r^2 = y_i y_i. \tag{11}$$

3.5 Numerical Implementation

Since no analytic solution can be found for the integral BEM equation (Eq. 6), a numerical approximation is sufficient. In order to obtain $\widetilde{BEP}$, the numerical solution scheme and the discretization for the BEP is discussed in this section. The scheme represented in Figure 2 is the process by which a numerical solution to $\widetilde{BEP}$ is found.

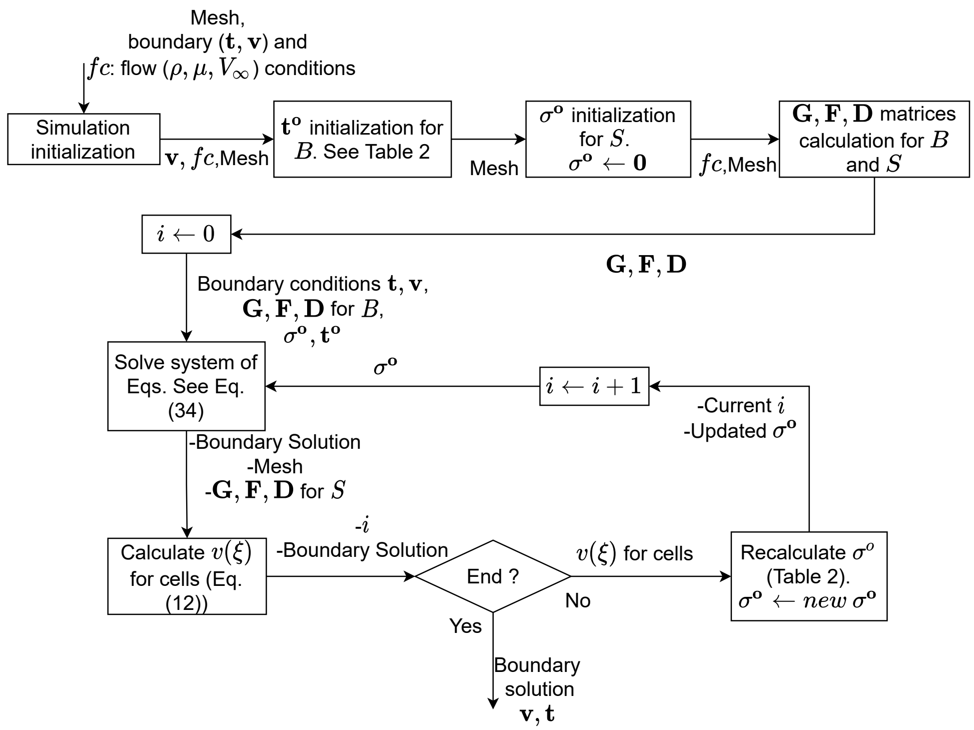

Figure 2: Flow chart for the general process to achieve a numerical solution for $\widetilde{BEP}$. fc: Flow conditions variables.

The end condition in Figure 2 can be met by one or both of the following conditions. The first being that a number of iterations is met. The second is accomplished when the difference of the boundary conditions between the $i-1$ and i iteration is less than a tolerance ϵ. For this manuscript both criteria are utilized but the iterative process is ended when a number of iterations is reached because it occurs prior to the convergence of the boundary conditions under a tolerance.

3.5.1 Spatial Discretization

The domain Ω for the BEP has to be discretized since the analytic continuous equation that represents it cannot be determined. B and S are discretized with the following elements:

- Boundary Elements: 1-dimensional constant elements (see Figure (3)). Defined by two geometrical nodes and one functional node (centroid).
- Surface Cells: 2-dimensional constant triangular cell elements (see Figure (3)). Defined by 3 geometrical nodes and one functional node (centroid).

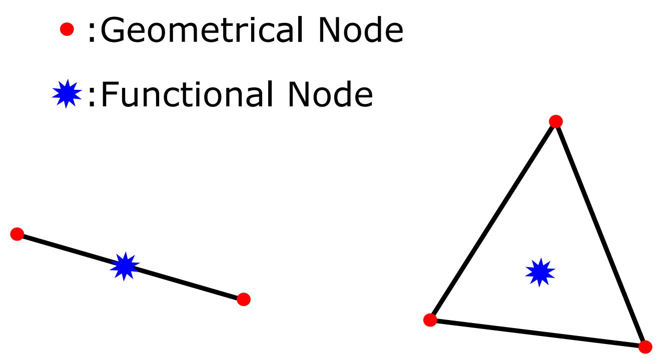

Figure 3: Boundary (left) and surface (right) elements.

3.5.2 Discretized BEM Equation [8]

Taking into account the spatial discretization defined in section 3.5.1, the Eq. (6) is reformulated in Eq. (12).

$$
\begin{aligned}
c_{ij} v_i(\xi) = \sum_{m=1}^{M} \left(t_i(Xm) \int_{B_m} G_{ij}(r) \mathrm{d}B - v_i(Xm) \int_{B_m} F_{ij}(r) \mathrm{d}B - t_i^o(Xm) \int_{B_m} G_{ij}(r) \mathrm{d}B \right) \\
+ \sum_{l=1}^{L} \sigma_{ki}^o(Xl) \int_{S_l} \frac{\partial G_{ij}(r)}{\partial x_k} \mathrm{d}S \,,
\end{aligned}
\tag{12}
$$

with M and L being the total number of boundary elements and surface cells. Descriptions for some terms of Eq. (12) can be seen in Table 4.

Table 4: Terms description for the Discretized BEM equation. T: Time units, L: Distance units, M: Mass units.

Term	**Description**	**Dims.**
$B = \sum_{m=1}^{M} B_m$.	Boundary discrete composition.	-
$S = \sum_{l=1}^{L} S_l$.	Non-linear convective region discrete composition.	-
$t_i^o = \rho(V_k + v_k) n_k v_i$.	Non-linear convective traction vector for boundary elements.	$\frac{M}{LT^2}$.
$\sigma_{ki}^o = \rho(V_k + v_k) v_i$.	Non-linear convective traction tensor for surface cells.	$\frac{M}{LT^2}$

3.6 Integral Approaches

The integrals contained in Eq. (12) are evaluated for all elements to obtain a linear system of equations in terms of unknown boundary conditions. Some of them are singular and some non-singular. For this, the current section presents an implementation of the method proposed by [2, 12] for the evaluation of the singular boundary integrals. In addition, a direct analytic evaluation is also discussed for the singular surface integrals as part of our contribution in the BEM solution for the specified flow.

3.6.1 Non-singular and Singular Situations for Boundary and Surface Elements

The boundary and surface integrals are solved for all combinations of $\vec{\xi}$ and $\vec{X}$, both positioned in boundary and surface elements. The positioning of $\vec{\xi}$ in the boundary elements (Figure 4) corresponds to the integration process needed to compute the missing boundary conditions. In addition, positioning $\vec{\xi}$ in the surface cells (Figure 5) is performed for integrals needed to recalculate σ^o in each iteration. Cases in which X and ξ are positioned in different topological entities (element and cell) are omitted in Figures (4, 5) since these are not singular.

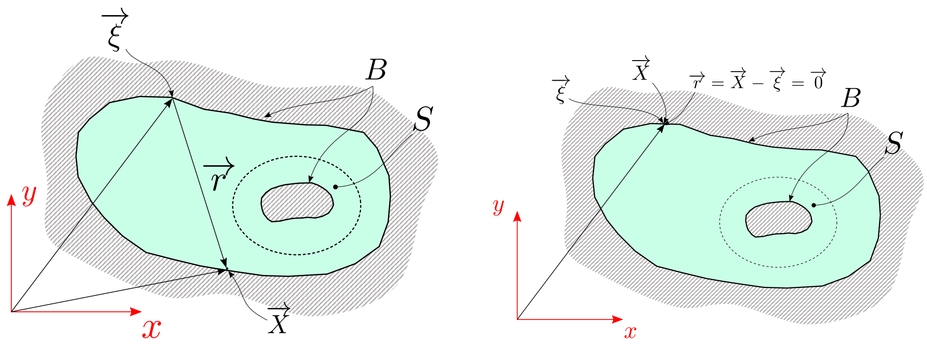

(a) (b)

Figure 4: Boundary (B) ξ and X elements positions for boundary integrals. Surface (S) is the relevant non-linear convection zone. (**a**) Non singular situation. ξ and X are not coincident. $\vec{r} = X - \xi \neq \mathbf{0}$. Numerical integration is applied for the mesh elements. (**b**) Singular situation. ξ and X are coincident. $\vec{r} = X - \xi = \mathbf{0}$. Situation for which our contribution is made. Analytic integration scheme is implement over a canonical element.

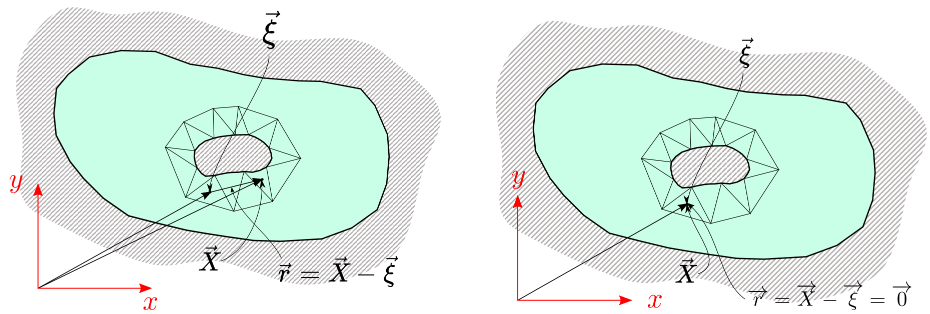

(a) (b)

Figure 5: Surface (S) ξ and X elements positions for surface integrals. Integral evaluation cases for the calculation of σ^o between iterations. (**a**) Non singular situation. ξ and X are not coincident. $\vec{r} = X - \xi \neq \mathbf{0}$. Numerical integration is applied for the mesh elements. (**b**) Singular situation. ξ and X are coincident. $\vec{r} = X - \xi = \mathbf{0}$. Situation for which our contribution is made. Direct analytic integration is performed over a canonical element.

3.6.2 Non-singular Boundary and Surface Integrals

For the non-singular cases $X \neq \xi$, the integration over the boundary and surface is computed numerically. A 3-point and 1-point Gaussian Quadrature are performed for boundary and surface integrals respectively. These numerical integrals are not treated or explained in detail since they are not the focus of this article.

3.6.3 Singular Boundary Integrals

For the singular boundary integrals ($\vec{\xi} = \vec{X}$), the computation is performed with the method presented in [2, 12]. The method consists in displacing the source node ξ a distance D (Figure 6). After displacement, the now non-singular boundary integrals can be evaluated analytically and the limit taken as $D \to 0^+$ (since D is a distance) as per Eqs. (13) and (14). A graphical explanation of the displacement is presented in Figure 6. The integration is performed over a canonical element (with size l of the real element) in its local coordinate system.

$$AIG_{ij}(X_m - \xi_m) = \lim_{D \to 0^+} \int_{B_m} G_{ij}(X_m - (\xi_m - D))dB. \tag{13}$$

$$AIF_{ij}(X_m - \xi_m) = \lim_{D \to 0^+} \int_{B_m} F_{ij}(X_m - (\xi_m - D))dB. \tag{14}$$

This method of displacement of the source node is presented by [2, 12] for the elasticity and fracture fields respectively. Our contribution consists in its implementation applied in the field of fluid dynamics described in section 1. In addition, a contribution is proposed as the direct analytic solution of the singular surface integrals (see section 3.6.4).

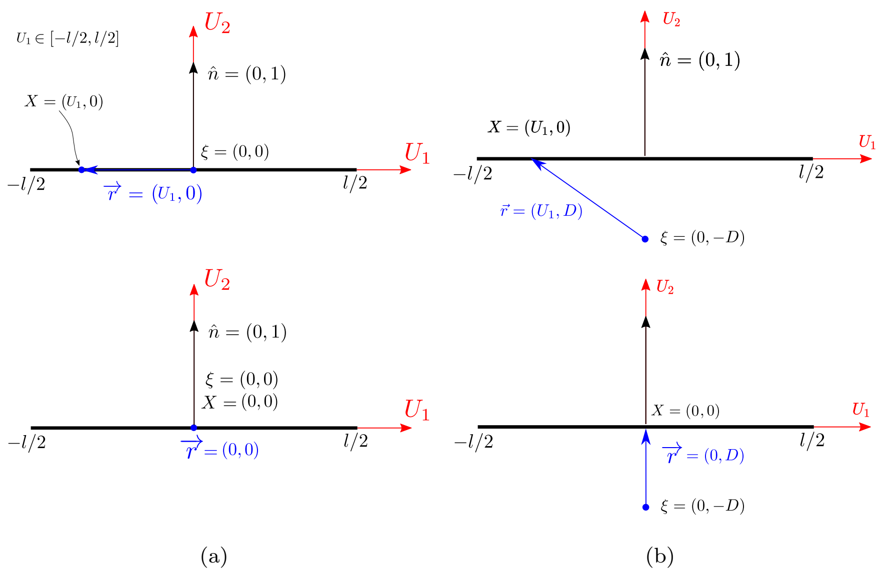

Figure 6: Analytic integration over the canonical singular element m (see Figure 4 (b)) $\xi = X_m$. Canonical coordinate system. Integrating for $U_1 \in [-l/2 \rightarrow l/2]$ in local canonical coordinates. Scenario (subfigure (**a**)) of our contribution. (**a**) Singular case occurs when $x = 0$. X and ξ coincide (bottom). (**b**) Displacement of source node (ξ) for the correction of the singular case. $\forall x, \vec{r} \neq \mathbf{0}$.

The mathematical procedure for avoiding the singularity (Figure 6 (a)) and the analytic integral evaluation is discussed next. The modified arguments of the Green functions (Eqs. 10 and 11) are presented in Eqs. (15-17). These are then replaced in each Green functions G_{ij} and F_{ij} as shown in Eqs. (18,24) for G_{11}, F_{11}.

$$y_1 = X_1 - \xi_1 = U_1 - 0 = U_1. \tag{15}$$

$$y_2 = X_2 - \xi_2 = 0 - (-D) = D. \tag{16}$$

$$r = \sqrt{U_1^2 + D^2}. \tag{17}$$

$$G_{11}(X - \xi, D) = \frac{1}{4\pi\mu}\left(\frac{U_1^2}{U_1^2 + D^2} - \ln\left(\sqrt{U_1^2 + D^2}\right)\right). \tag{18}$$

The result of integrating this modified function is presented in Eq. (19). Following the same procedure, the results for the integrands G_{12}, G_{21} and G_{22} are presented in Eqs. (20-22).

$$\lim_{D\to 0^+} \frac{1}{4\pi\mu} \int_{-l/2}^{l/2} \frac{U_1^2}{U_1^2+D^2} - \ln\left(\sqrt{U_1^2+D^2}\right) dU_1 = \frac{l\left(-\ln\left(l^2\right)+\ln\left(4\right)+4\right)}{8\mu\pi}. \tag{19}$$

$$\lim_{D\to 0^+} \int_{-l/2}^{l/2} G_{12}(X-\xi, D) dU_1 = 0. \tag{20}$$

$$\lim_{D\to 0^+} \int_{-l/2}^{l/2} G_{21}(X-\xi, D) dU_1 = 0. \tag{21}$$

$$\lim_{D\to 0^+} \int_{-l/2}^{l/2} G_{22}(X-\xi, D) dU_1 = \frac{l\left(-\ln\left(l^2\right)+\ln\left(4\right)+2\right)}{8\mu\pi}. \tag{22}$$

Furthermore, to solve $AIF_{ij}(X_m-\xi_m)$, one has that the normal vector $\hat{n}$ of the canonical element is,

$$n_1 = 0, \quad n_2 = 1. \tag{23}$$

Now, taking into account the normal vector, the variables in Eqs. (15-17) are replaced for the integrands F_{ij} as seen in Eq. (24) for F_{11}. The integration is then performed as expressed in Eq. (14). This is shown in Eqs. (25-28).

$$F_{11}(X-\xi, D, \hat{n}) = \frac{1}{2\pi}\left(\frac{2U_1^2 D}{(U_1^2+D^2)^2}\right). \tag{24}$$

$$\lim_{D\to 0^+} \frac{2}{2\pi} \int_0^{l/2} \frac{2U_1^2 D}{(U_1^2+D^2)^2} dU_1 = \frac{1}{2}. \tag{25}$$

$$\lim_{D\to 0^+} 2 \int_0^{l/2} F_{22}(X-\xi, D, \hat{n}) dU_1 = \frac{1}{2}. \tag{26}$$

$$\lim_{D \to 0^+} \int_{-l/2}^{l/2} F_{12}(X - \xi, D, \hat{n}) dU_1 = 0. \tag{27}$$

$$\lim_{D \to 0^+} \int_{-l/2}^{l/2} F_{21}(X - \xi, D, \hat{n}) dU_1 = 0. \tag{28}$$

For the integrals of F_{12} and F_{21}, the result is nule since this functions are odd with respect to 0. The results obtained in Eqs. (19-22) and (25-28) are transformed (see section 3.6.5) and stored in matrices AIG^m and AIF^m. These matrices compose the diagonal band of the influence matrices **G** and **F** (see section 3.6.6).

3.6.4 Singular Surface Integrals

As expressed in Figure 5, the surface integral evaluation presents a singularity when $\xi = X$ (see also Figure 7). This occurs only for the integration needed to calculate $v(\xi)$ (recalculation of σ^o) in each new iteration (see subsection 3.8). Even though the singularity is present in the Green function $\frac{\partial G_{ij}}{\partial x_k}$, the integral exists and is bounded. Consequently, an analytic integration without avoiding the singularity is performed over a canonical element (Figure 8) and then transformed for the real element.

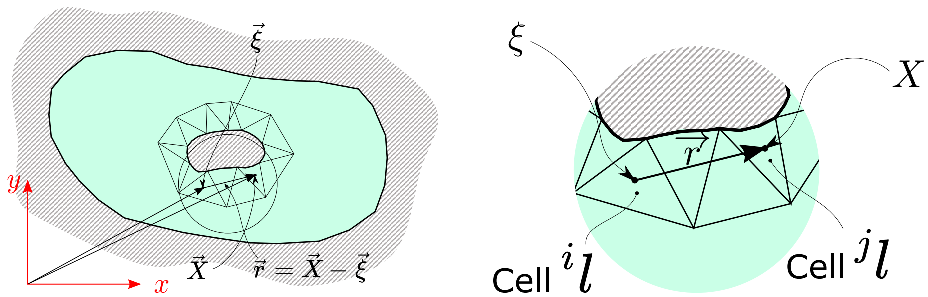

(a) (b)

Figure 7: General integration case for region S. Singularity occurs when $i = j$ (triangles ^{i}l and ^{j}l coincide) and points ξ and X are coincident ($\vec{r} = \mathbf{0}$). (**a**) General surface integration case. Selected cells ^{j}l (X) and ^{i}l (ξ). (**b**) Selected region in Figure 7(a).

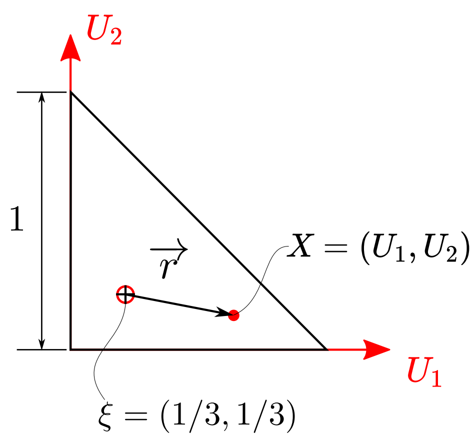

Figure 8: Canonical element (axis U_1, U_2). Domain for the analytic integration of $\frac{\partial G_{ij}(X-\xi)}{\partial U_k}$. Scenario of our contribution.

Since the function $\frac{\partial G_{ij}(X-\xi)}{\partial U_k}$ has a reflection with respect to the singularity point $\xi = X$ in the canonical element, the integral of such function exists and has a bounded value. The integration is performed in SymPy [16] with the integrate() method. The results of such integration are given in Table 5. Since $\int\limits_{S_m} \frac{\partial G_{12}}{\partial x_k} dS_m = \int\limits_{S_m} \frac{\partial G_{21}}{\partial x_k} dS_m$, the result for the integrands $\frac{\partial G_{12}}{\partial x_k}$ are the only ones shown.

Table 5: Results for singular surface integrals of $\frac{\partial G_{ij}}{\partial U_k}$. Results for canonical element (see Figure 8). SymPy [16] used for integral evaluation. Results given in symbolic format as per SymPy display.

Analytic Integral Equation	**Result**	**Observations**
$I_a\frac{\partial G_{11}}{\partial U_1} = \int_0^1\int_0^{1-U_1}\frac{\partial G_{11}(X-\xi)}{\partial U_1}dU_2dU_1$	$-\frac{-3+\ln(\frac{5}{2})+2\tan^{-1}(3)}{24\mu\pi}$	Results are transformed (see Eq. 33) and assembled in ${}^oI_a\partial G$ (see Figure 12).
$I_a\frac{\partial G_{12}}{\partial U_1} = \int_0^1\int_0^{1-U_1}\frac{\partial G_{12}(X-\xi)}{\partial U_1}dU_2dU_1$	$\frac{-3+\ln(\frac{5}{2})+2\tan^{-1}(3)}{24\mu\pi}$	
$I_a\frac{\partial G_{22}}{\partial U_1} = \int_0^1\int_0^{1-U_1}\frac{\partial G_{22}(X-\xi)}{\partial U_1}dU_2dU_1$	$-\frac{3-2\pi+\tan^{-1}(\frac{117}{44})+\ln(\frac{5}{2})}{(24\pi\mu)}$	
$I_a\frac{\partial G_{11}}{\partial U_2} = \int_0^1\int_0^{1-U_1}\frac{\partial G_{11}(X-\xi)}{\partial U_2}dU_2dU_1$	$-\frac{3-2\pi+\tan^{-1}(\frac{117}{44})+\ln(\frac{5}{2})}{(24\pi\mu)}$	
$I_a\frac{\partial G_{12}}{\partial U_2} = \int_0^1\int_0^{1-U_1}\frac{\partial G_{12}(X-\xi)}{\partial U_2}dU_2dU_1$	$\frac{-3+\ln(\frac{5}{2})+2\tan^{-1}(3)}{24\mu\pi}$	
$I_a\frac{\partial G_{22}}{\partial U_2} = \int_0^1\int_0^{1-U_1}\frac{\partial G_{22}(X-\xi)}{\partial U_2}dU_2dU_1$	$-\frac{-3+\ln(\frac{5}{2})+2\tan^{-1}(3)}{24\mu\pi}$	

3.6.5 Transformations to the Real Elements for Boundary and Surface Analytic Integrals

The results of the singular integrals, both for boundary and surface elements, are obtained for canonical elements. Therefore, these results must be mapped from a canonical domain to the real domain of the $\widetilde{BEP}$. The transformations that perform such mapping are discussed next for each element type (boundary-surface).

Boundary Elements Transformation

For the boundary integrals, a tensor transformation of the results of Eqs. (13) and (14) is performed. This transformation is computed with a transformation matrix N (Eq. 29), which is calculated for each element with the components n_i of its normal vector $\hat{n}$. See Figure 9 for a graphical representation of the element orientation in both coordinate systems.

$$N = \begin{bmatrix} \cos\alpha & -\sin\alpha \\ \sin\alpha & \cos\alpha \end{bmatrix} = \begin{bmatrix} n_2 & -n_1 \\ n_1 & n_2 \end{bmatrix}. \tag{29}$$

The transformation in Eqs. (30-31) represents the tensors AIG_{ij} and AIF_{ij} in the $x\,y$ coordinates.

$$^{o}AIG_{ij} = N^T AIG_{ij} N. \tag{30}$$

$$^{o}AIF_{ij} = N^T AIF_{ij} N. \tag{31}$$

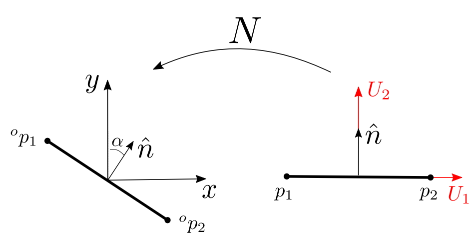

Figure 9: Boundary element in canonical and real orientation. Canonical $(U_1\,U_2)$ and real $(x\,y)$ coordinate systems.

Surface Elements Transformation

The analytic integration is executed over a canonical constant triangular element, as shown in Fig 8. Therefore a transformation to the real domain (see Figure 10) is needed. This transformation $T : \Omega_c \rightarrow \Omega_r$ is affine. Therefore, the Jacobian that represents such transformation is constant for each element.

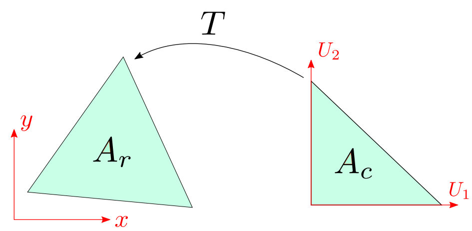

Figure 10: Transformation from canonical element (right) to mesh element (left).

Since the Jacobian is constant for each element, the determinant is the same at each point, and it can be calculated as the ratio of the areas. Eq. (33) presents an example on how the transformation of the integral is applied.

$$|J| = \frac{A_r}{A_c}. \tag{32}$$

$$^{o}AI\frac{\partial G_{ij}}{\partial x_k} = |J|AI\frac{\partial G_{ij}}{\partial U_k}. \tag{33}$$

3.6.6 Boundary and Surface Influence Matrices Assembly

Influence matrices $\mathbf{G}, \mathbf{F}, \mathbf{D}$ are assembled for the system of equations (Eq. 12) to be written in matrix form (Eq. 34). These are represented as block matrices for ease of understanding. Each row i contains all results of integrals for ξ_i w.r.t each X_j, $j = 1, 2, ..., M$.

Boundary and Surface Matrices

$\mathbf{G}, \mathbf{F}, \mathbf{D}$ are needed in two processes -solution of system of equations (Eq. 34), recalculation of $v(\xi)$ for cells (S) in each iteration (see Figure 2). For the first case, the matrices coefficients correspond to the results of integrals with ξ placed in B. For the second case, ξ is placed in S. For both cases X is placed in B for $\mathbf{G}, \mathbf{F}$ or in S for $\mathbf{D}$.

Assembly of Matrices

The composition of $\mathbf{G}$ is shown in Figure 11. The positions in the diagonal $(i = j)$ correspond to the transformed results of the singular integrals (Eqs. 30) of $G_{ij}(X-\xi)$. This if ξ and X lie in the same element. Otherwise, the coefficients of the diagonal correspond to non-singular integrals (see section 3.6.2). In any case, the non-diagonal terms ($i \neq j$) correspond to non-singular integrals.

For **F**, the assembly is identical to **G** (see Figure 11). The exception being that the coefficients correspond to the transformed results from the integrals of $F_{ij}(\xi - X_m, \hat{n})$ and the contribution of the diagonal matrix c (see Table 4). For **G** and **F**, the sub-matrices ${}^{o}AIG^{m}$ and ${}^{o}AIF^{m}$ are of size 2×2.

$$\mathbf{G} = \begin{array}{c} \\ \xi_1 \\ \xi_2 \\ \vdots \\ \xi_M \end{array} \begin{array}{c} \begin{array}{cccc} X_1 & X_2 & \dots & X_M \end{array} \\ \begin{bmatrix} {}^{o}AIG^{1} & & & \\ & {}^{o}AIG^{2} & & \\ & & \ddots & \\ & & & {}^{o}AIG^{M} \end{bmatrix}_{2M \times 2M} \end{array}$$

Figure 11: Matrix **G** composition. Block matrix representation. Results from boundary integration of $G(X-\xi)$.

For **D**, the assembly is similar to both of **G** and **F**. The difference relies in the assembly of the sub-matrices ${}^{o}AI\partial G$ shown in Figure 12 (b). When $u(\xi)$ is calculated in each iteration, the diagonal sub-matrices (Figure 12) of **D** are composed of the values in Table 5.

$$
\mathbf{D} = \begin{array}{c c} & \begin{array}{cccc} X_1 & X_2 & \dots & X_L \end{array} \\ \begin{array}{c} \xi_1 \\ \xi_2 \\ \vdots \\ \xi_L \end{array} & \begin{bmatrix} {}^{o}AI\partial G^{1} & & & \\ & {}^{o}AI\partial G^{2} & & \\ & & \ddots & \\ & & & {}^{o}AI\partial G^{L} \end{bmatrix}_{2L \times 4L} \end{array}
$$

(a) Influence matrix $\mathbf{D}$

$$
{}^{o}AI\partial G^{l} = \begin{bmatrix} {}^{o}AI\frac{\partial G_{11}}{\partial x_1}^{l} & {}^{o}AI\frac{\partial G_{12}}{\partial x_1}^{l} & {}^{o}AI\frac{\partial G_{21}}{\partial x_1}^{l} & {}^{o}AI\frac{\partial G_{22}}{\partial x_1}^{l} \\ {}^{o}AI\frac{\partial G_{11}}{\partial x_2}^{l} & {}^{o}AI\frac{\partial G_{12}}{\partial x_2}^{l} & {}^{o}AI\frac{\partial G_{21}}{\partial x_2}^{l} & {}^{o}AI\frac{\partial G_{22}}{\partial x_2}^{l} \end{bmatrix}
$$

(b) Sub-matrix ${}^{o}AI\partial G$ composition for cell m

Figure 12: Matrix $\mathbf{D}$ composition. Block matrix representation. Results from surface integration of $\frac{\partial G(X-\xi)}{\partial x}$.

3.7 System of Equations

The $\widetilde{BEP}$ results in a linearized system of equations so that the unknown boundary conditions can be found in an iterative process. The evaluation of Eq. (12) for all elements in B ($\xi_i,\ i = 1, 2, ..., M$), produces this system. It is written in matrix form as follows (see also Figure 13).

$$
\mathbf{Gt} - \mathbf{Fv} - \mathbf{Gt^{o}} + \mathbf{D}\sigma^{\mathbf{o}} = \mathbf{0}. \tag{34}
$$

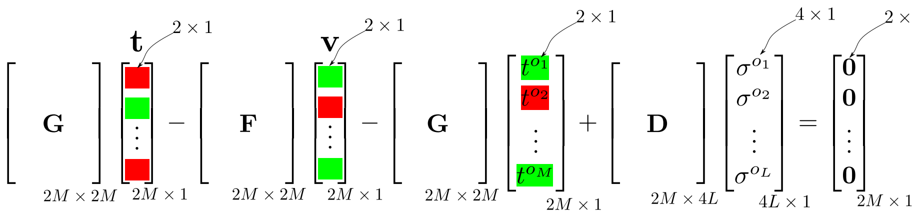

Figure 13: System of equations (Eq. 34). *Known* Boundary Conditions (green). *Unknown* Boundary Conditions (red). M: Total number of B elements. L: Total number of S cells. Vector $\mathbf{t^o}$ depends on the *Known* and *Unknown* terms of the boundary $\mathbf{v}$.

Eq. 34 can be reorganized and rewritten in terms of a vector of *unknowns* $\mathbf{x}$ and a vector of *known* boundary conditions $\mathbf{y}$,

$$\mathbf{g}(\mathbf{x}) = \mathbf{Ax} - \mathbf{D}\sigma^{\mathbf{o}} + \mathbf{Gt^o} - \mathbf{By} = \mathbf{0}. \tag{35}$$

, for which matrix $\mathbf{A}(\mathbf{G}, \mathbf{F}, \mathbf{t}, \mathbf{v})$ corresponds to *unknown* boundary conditions. Matrix $\mathbf{B}(\mathbf{G}, \mathbf{F}, \mathbf{t}, \mathbf{v})$ corresponds to *known* boundary conditions. Eq. 35 is solved to obtain the solution in the boundary.

3.8 Iterative Process

An iterative process is necessary due to the assumption that $\rho u_j \frac{\partial u_i}{\partial x_j}$ is known for the linearization of Eq. (5). This linearization allows the formulation of the BEM integral equation and then iterated over σ^o_{ki} to converge the unknown boundary values.

The iterative process initializes $\sigma^o_{ki} = 0$. Then, at each iteration i, the boundary values are calculated and σ^o_{ki} is updated according to these new results. $u_i(\xi)$ is calculated with the new Boundary Conditions for recalculation of σ^o_{ki}.

The iterative process is terminated once the tendency of convergence is observed in the boundary solution. This happens when the fluctuations between states of iteration i and $i-1$ are insignificant. Since the convergence can not be ensured, a specific number of iterations are performed. This number of iterations is determined arbitrarily and the convergence behavior is observed.

4 Results

4.1 Comparison of Singular Integrals Results

A comparison of the results of the singular boundary integrals of Eqs. (7-8) is observed in this section. These are computed for boundary canonical elements (Figure 6) with the method presented in this manuscript and the method presented in Ref. [1]. These elements have a size of $l = 2$, with $x \in [-1, 1]$. μ is assumed unitary, $\mu = 1$.

Table 6: Singular boundary integral results for Green functions $G_{ij}(X - \xi)$ and $F_{ij}(X - \xi)$. Integration over canonical boundary element.

Integrand	**Source Node Displacement [2, 12] (Our implementation)**	**Distortion Method [1]**
G_{11}	$\frac{1}{\pi}$	0
G_{12}	0	0
G_{21}	0	0
G_{22}	$\frac{1}{2\pi}$	0
F_{11}	0.5	0.5
F_{12}	0	0
F_{21}	0	0
F_{22}	0.5	0.5

Refs. [6, 8] do not provide details for items such as (1) quadrature scheme utilized, (2) number of integration points, (3) 2-dimensional alternative chosen in the case of [6], (4) domain mapping. Because of these and the fact that they do not specify their procedure nor provide their results for the singular boundary integrals, these cannot be reproduced for comparison. Nevertheless, it does not mean the general procedure and results obtained by [6, 8] are questioned. We state that we do not have sufficient information to reproduce the mentioned results for our specific case.

The null values obtained for the singular integrals of G_{ij}, in the case of the distortion method [1], are obtained directly from that manuscript. In appendix B it is said that, "But for the boundary integral I_2 (2.34), which has a removable singularity of order $(\ln r)$, its contribution along the bumped part around the singularity will be exactly zero." [1]. Since no additional information or explanation is provided, the interpretation leads to the result presented in Table 6. We do not have further information regarding these discrepancies.

In addition to the results presented in Table 6, the analytic result for the integral of G_{ij}, without avoiding the singularity, is given in Table 7 to compare with the result obtained with the Source Node Displacement method. This comparison is shown because of the discrepancy found between the Source Node Displacement method and the Distorsion method. This result is obtained by integrating analytically the same canonical element for Table 6. The integrand G_{ij} is not modified and is assumed as per Equation 7. The analytic integrals for G_{11} and G_{22} are expressed in Equations 36 and 37 .

$$\frac{1}{\pi}\int_{-1}^{1}(1-\ln\sqrt{x^2})\mathrm{dx}. \tag{36}$$

$$\frac{1}{\pi}\int_{-1}^{1}(-\ln\sqrt{x^2})\mathrm{dx}. \tag{37}$$

Table 7: Singular boundary integral results for Green function $G_{ij}(X-\xi)$. Integration over canonical boundary element. Source Node Displacement method and analytic integral without avoiding the singularity.

Integrand	**Source Node Displacement [2, 12] (Our implementation)**	**Analytic Integral Result Without Avoiding the Singularity**
G_{11}	$\frac{1}{\pi}$	$\frac{1}{\pi}$
G_{12}	0	0
G_{21}	0	0
G_{22}	$\frac{1}{2\pi}$	$\frac{1}{2\pi}$

From Table 7 it can be seen that the approximation of the singular integral of G_{ij} by means of the Source Node Displacement method is correct. The integral results for the F_{ij} function were not computed by an analytic evaluation. This is because the results found by the source node displacement method were already compared and found equal to the ones found in the Distortion Method [1].

4.2 Numerical Examples

The numerical examples discussed next are solved using the Boundary Method formulated previously. This examples are used to test the approximation with the analytic solutions of the singular integrals. The results are obtained with an implementation in Python of the numerical solution of BEM presented in section 3. This implementation is developed by the research team specifically for a free flow case with constant velocity V_i (free flow velocity).

Domain Discretization

Discretization of the boundary B and the region S, for each example (Figures 15- 19), is exhibited in this section. Elements used for discretization of the boundary and interior are discussed in section 3.5.1. For the examples in Figures 15-19, the domains (Ω's) are unbounded. External boundary Γ_0 to Ω does not exist. For these, only a region around S is evaluated in order to observe the flow's behavior around the submerged object. Figure 14 displays an indication of the angle of attack corresponding to Figs.15-16.

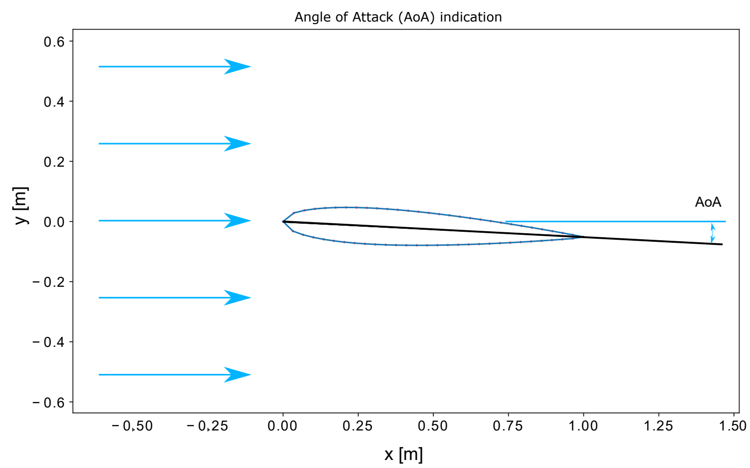

Figure 14: Indication of the angle of attack for the airfoils.

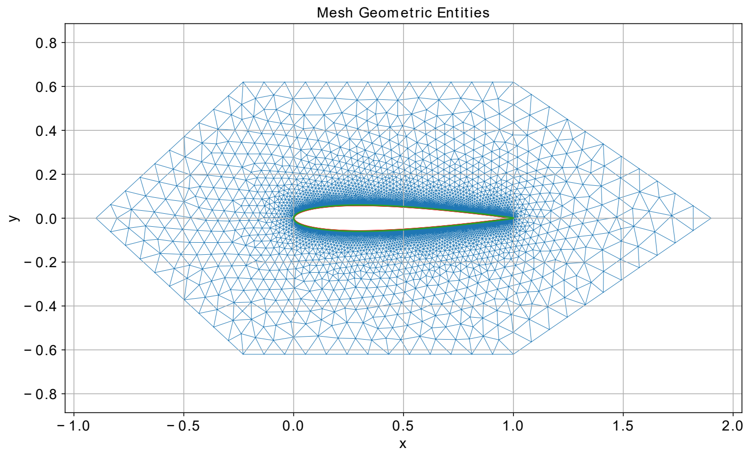

Figure 15: Mesh of airfoil at $\mathbf{0}^{\circ}$ angle of attack.

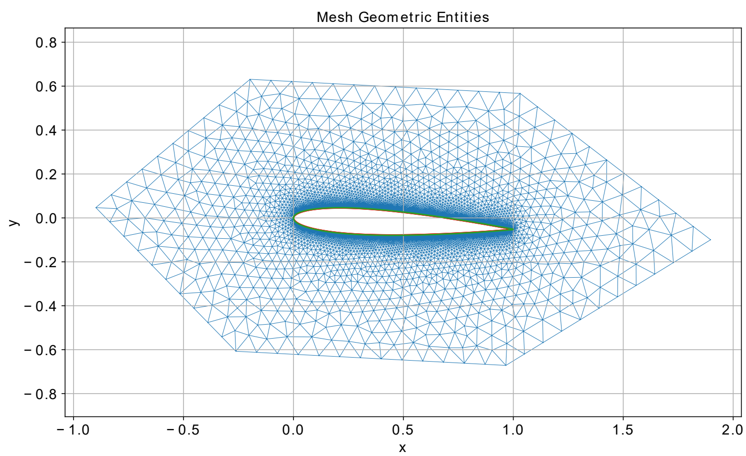

Figure 16: Mesh of airfoil at $\mathbf{3}^{\circ}$ angle of attack.

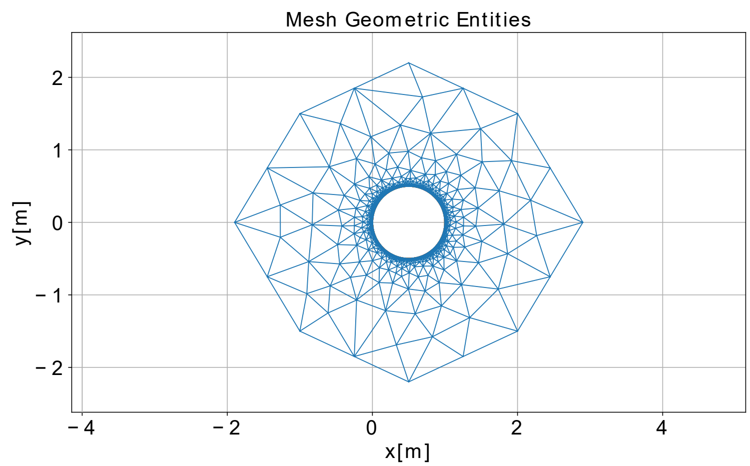

Figure 17: Mesh of 0.5 m radius circle. 2000 boundary elements. 7866 cell elements.

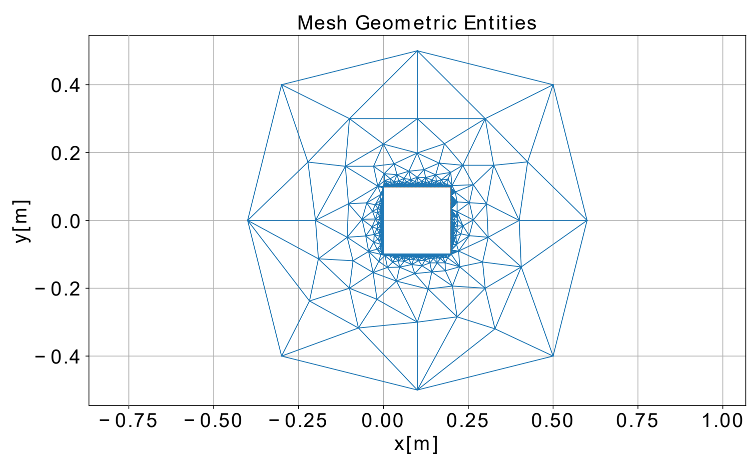

Figure 18: Mesh of 0.2 m side square. 2001 boundary elements. 4445 cell elements.

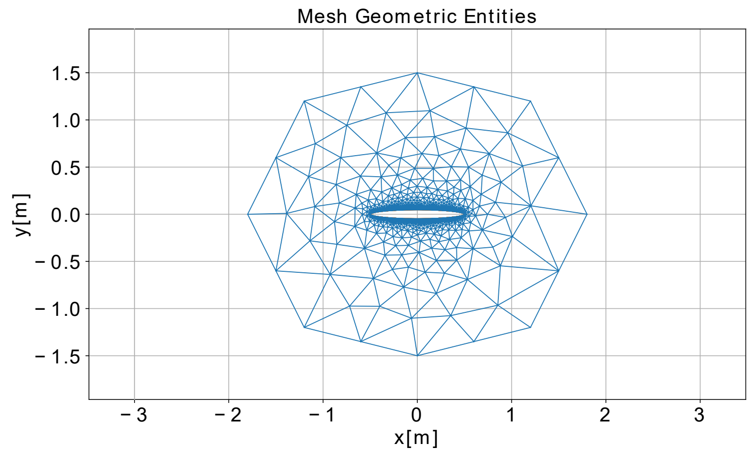

Figure 19: Mesh of ellipse. 2000 boundary elements. 11976 cell elements.

Flow Conditions/Fluid Properties.

The flow conditions and fluid properties used for the simulation of the numerical examples are presented in Table 8. The free flow velocity $V_1(Re, \nu, c)$ is different for each example. It depends on the characteristic length c of each submerged object.

$\rho[\frac{\mathrm{kg}}{\mathrm{m}^3}]$	$\mu[\frac{\mathrm{m}^2}{\mathrm{s}}]$	$\nu[\frac{\mathrm{kg}}{\mathrm{ms}}]$	Re	$V_1[\frac{\mathrm{m}}{\mathrm{s}}]$	$V_2[\frac{\mathrm{m}}{\mathrm{s}}]$
1.225	1.81×10^{-5}	1.48×10^{-5}	2	$V_1(Re, \nu, c)$	0

Table 8: Flow conditions. Fluid properties. V_1: free flow velocity in x direction. V_2: free flow velocity in y direction.

Boundary conditions.

The boundary conditions are assigned solely to the boundaries Γ_i. For every example's Γ_i, a No-slip condition is defined as a Dirichlet boundary condition $u_i(\Gamma) = 0$. Consequently, the traction $t(\Gamma)$ is *unknown*. In addition, σ^o is initialized as a null vector.

4.3 Integral Coefficients Results for Green Functions $G_{ij}(X-\xi)$ and $F_{ij}(X-\xi)$.

The integral coefficients for Green Functions $G_{ij}(X-\xi)$ and $F_{ij}(X-\xi)$ are presented for the mesh in Figure 15. These results are given in order to observe the behavior of the singular (analytic) and non-singular (numerical) integrals along the boundary. In addition, these results provide insight on the tendency of the non-singular integrals and how the singular integral fits in this tendency.

Three elements are selected (see Figure 20) for observation. It should be noticed that elements ξ_1 and ξ_{1000} are neighbors. This is worth mentioning because of the way the elements and their corresponding integral results are displayed in Figures 21 and 22. In addition, each curve (blue, yellow and green) corresponds to the integral coefficient results (analytic and numerical) of the evaluation of the selected elements (ξ_1, ξ_{300} and ξ_{500}) w.r.t all other elements in the boundary. This evaluation is for green functions G_{ij} and F_{ij}.

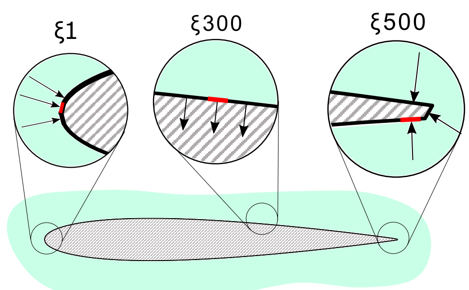

Figure 20: Selected neighbourhoods normals for Figures 21 and 22.

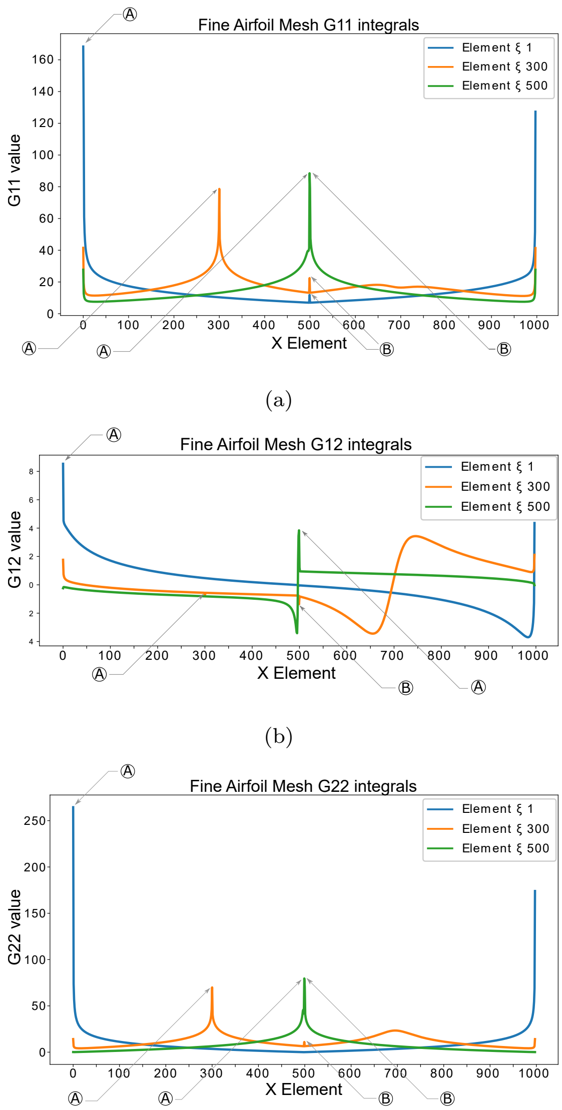

(a)

(b)

(c)

Figure 21: Analytic and numerical results for the integrals of Green function G. Airfoil at $\mathbf{0}°$ angle of attack (mesh in fig 15). A: Result of analytic integration for singular case in the boundary. B: C^0 Discontinuity produced by neighbourhood with strong normal changes. (**a**) $G_{11}(X-\xi)$. (**b**) $G_{12}(X-\xi)$. (**c**) $G_{22}(X-\xi)$.

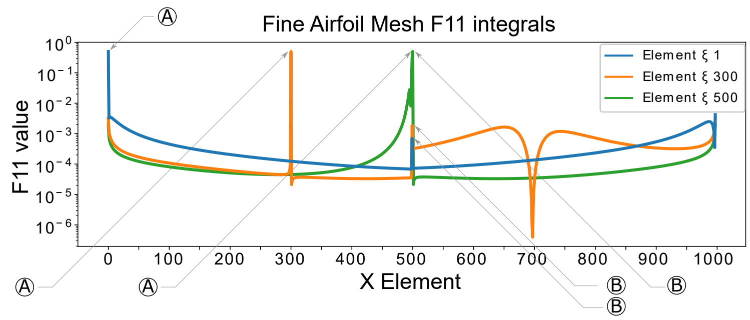

(a)

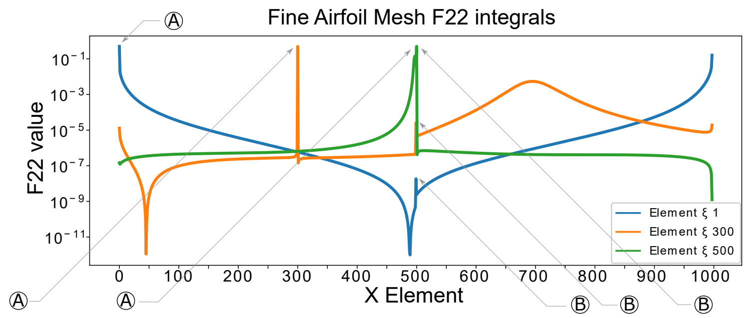

(b)

Figure 22: Analytic and numerical results for the integrals of Green function F. Airfoil at $\mathbf{0}^{\circ}$ angle of attack (mesh in fig 15). A: Result of analytic integration for singular case in the boundary. B: C^0 Discontinuity produced by neighbourhood with strong normal changes. (**a**) $F_{11}(X-\xi,\hat{n})$. (**b**) $F_{22}(X-\xi,\hat{n})$.

For Figures 21 and 22 the integral values at extremes $X = 1$ and $X = 1000$ correspond to neighboring elements in which a continuity of the results' tendency can be seen. As a consequence, a peak can be seen in element $X = 1000$ for the $\xi = 1$ curves. In addition, the peaks in the curves marked with (A) correspond to the analytic results of the singular integrals ($\xi = X$). Moreover, other peaks can be seen near the element $X = 500$ (marked with B) in Figures 21 and 22. This correspond to numerical (non-singular) integrals for $\xi = 1$ and $\xi = 300$. The specific case $X = \xi = 500$ is marked with (A) and (B) because the result corresponds to an analytic integration due to the singularity and the element belongs to a neighbourhood with strong normal changes, respectively.

Even though C^1 discontinuities can be seen at neighborhoods with strong geometric changes ($\hat{n}_m \cdot \hat{n}_{m+1} << 1$), they do not affect in any means the approximation of the singular integrals. They are mentioned because of their implication in the integral behavior. These discontinuities produce a peak in the integrals at the selected points (B) in Figures 21 and 22. These geometric discontinuities are a normal part of the example's discretization. They may or may not induce problems in the simulations but are not treated since it has no relation with the computation of the singular integrals, which is the focus of the manuscript.

4.4 Velocity Vector Field u_i

The velocity vector field u_i is observed in the vicinity of the submerged objects as shown in Figures (23-25). The prediction of the flow is obtained with the BEM procedure presented in Section 3 for a number of 40 iterations. These results are provided in order to observe the behavior of the numerical computation with the proposed approximation of the singular integrals. Meshes in Figures (17) and (19) have no velocity vector field results. This is caused by divergence in the *unknown* boundary conditions (see section 4.5).

(a)

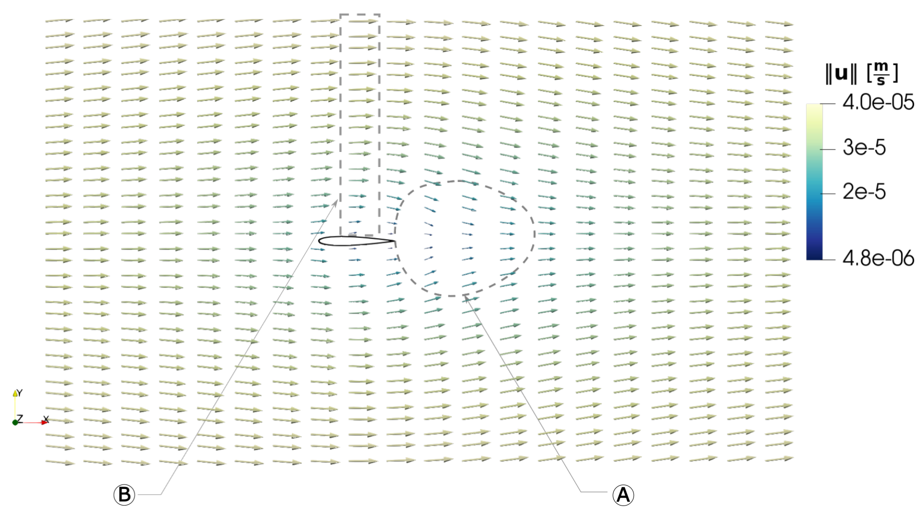

(b)

Figure 23: $\vec{u}(x, y)$ results for vicinity of airfoil at $\mathbf{0}°$ Angle of Attack. Simulation: Python/ANSYS, visualization: ParaView. (**a**) ANSYS simulation. A: observation region for post-obstruction flow. B: observation region for velocity gradient. (**b**) BEM simulation. A: observation region for post-obstruction flow. B: observation region for velocity gradient.

(a)

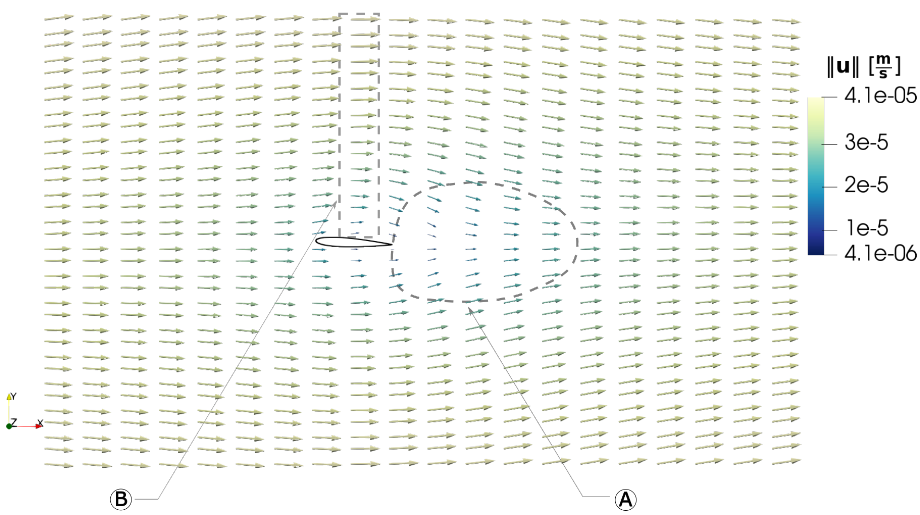

(b)

Figure 24: $\vec{u}(x, y)$ results for vicinity of airfoil at $\mathbf{3}^{\circ}$ Angle of Attack. Simulation: Python/ANSYS, visualization: ParaView. (**a**) ANSYS simulation. A: observation region for post-obstruction flow. B: observation region for velocity gradient. (**b**) BEM simulation. A: observation region for post-obstruction flow. B: observation region for velocity gradient.

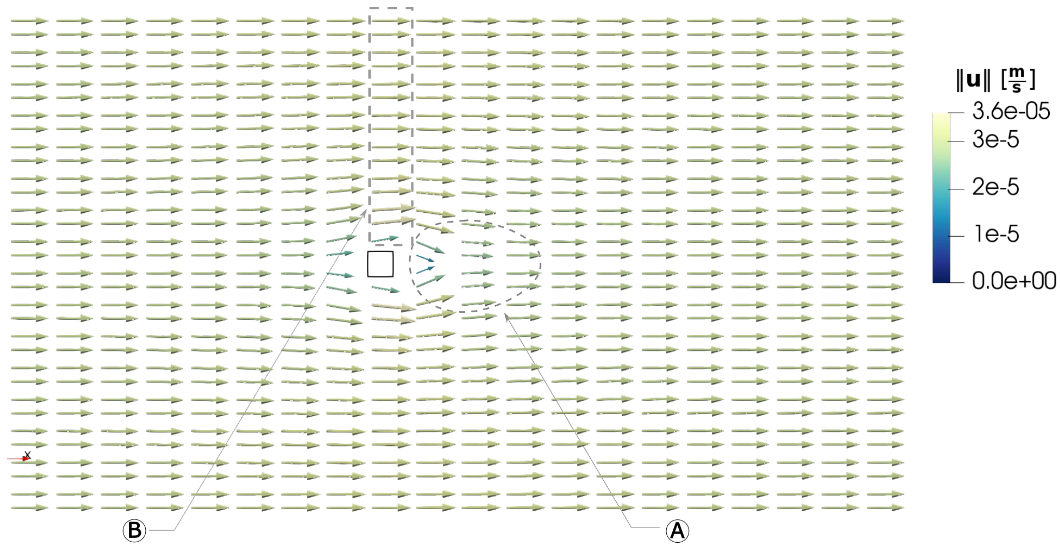

(a)

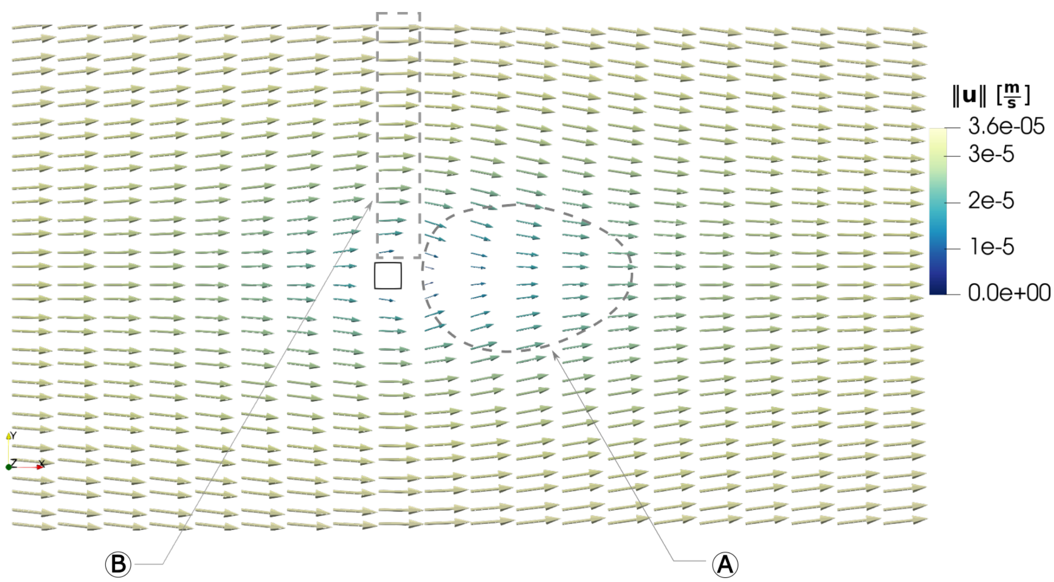

(b)

Figure 25: $\vec{u}(x, y)$ results for $0.1m$ side square vicinity. Simulation: Python/ANSYS, visualization: ParaView. (**a**) ANSYS simulation. A: observation region for post-obstruction flow. B: observation region for velocity gradient. (**b**) BEM simulation. A: observation region for post-obstruction flow. B: observation region for velocity gradient.

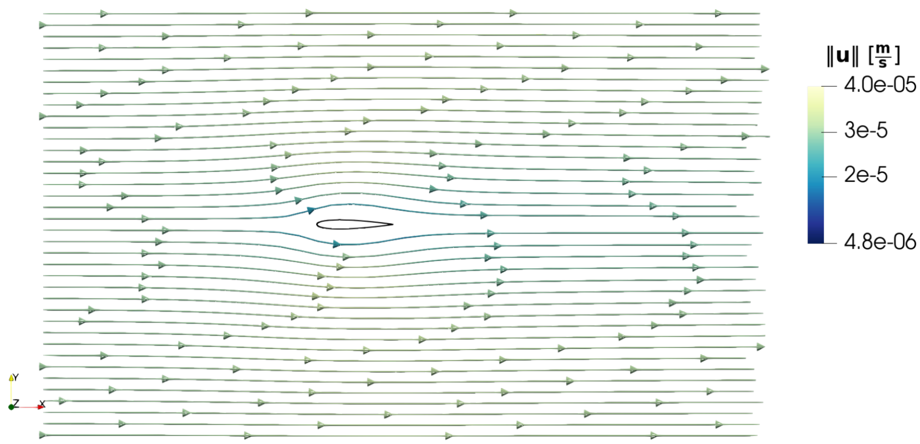

(a)

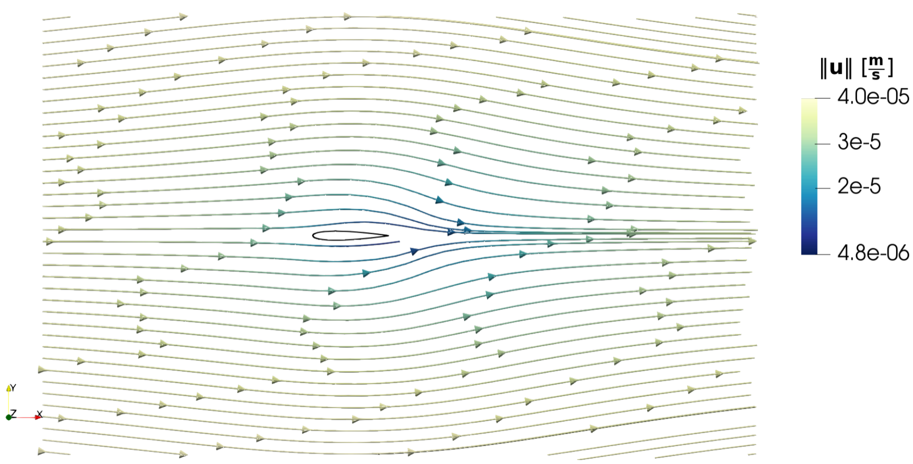

(b)

Figure 26: Absolute velocity streamlines results for vicinity of airfoil at $\mathbf{0}°$ Angle of Attack. Simulation: Python/ANSYS, visualization: ParaView. (**a**) ANSYS simulation. (**b**) BEM simulation.

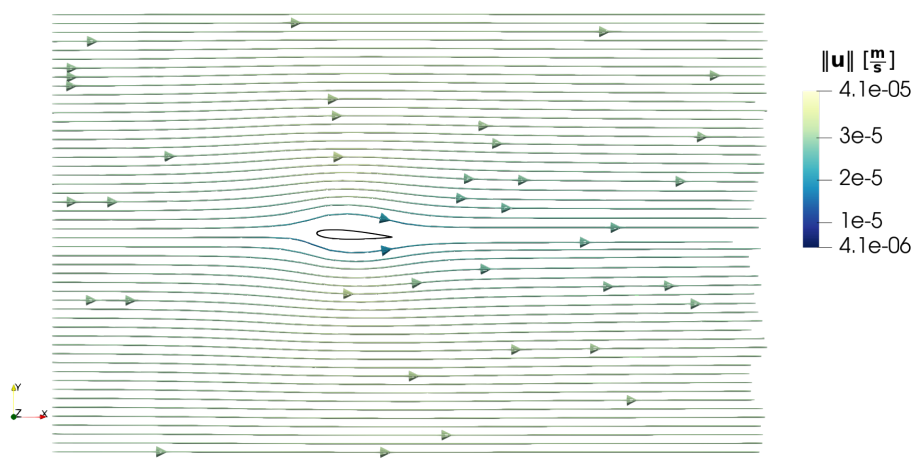

(a)

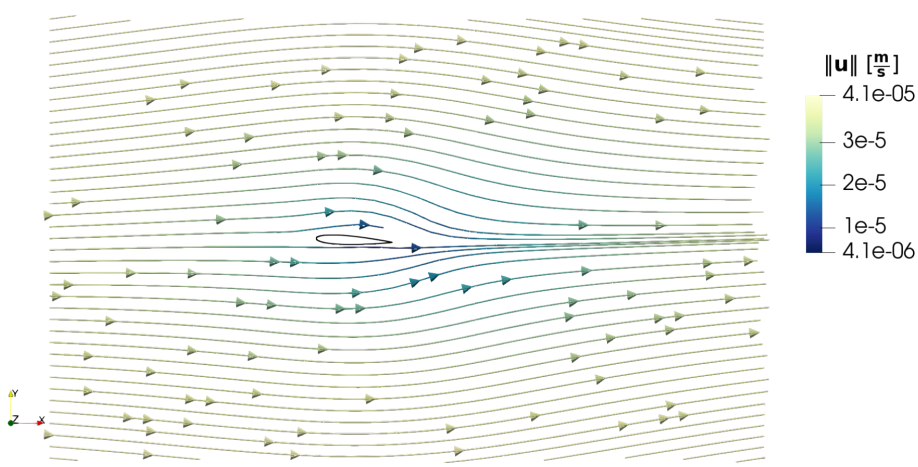

(b)

Figure 27: Absolute velocity streamlines results for vicinity of airfoil at **3**° Angle of Attack. Simulation: Python/ANSYS, visualization: ParaView. (**a**) ANSYS simulation. (**b**) BEM simulation.

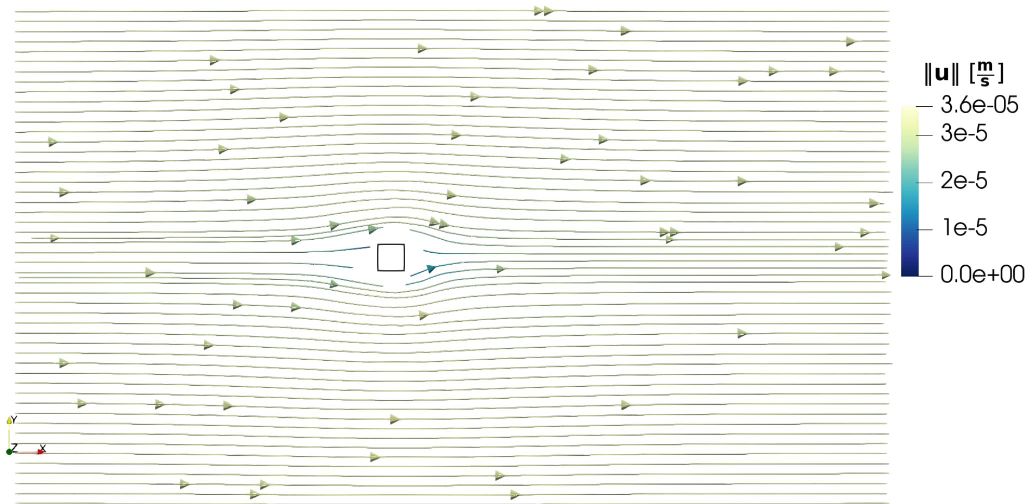

(a)

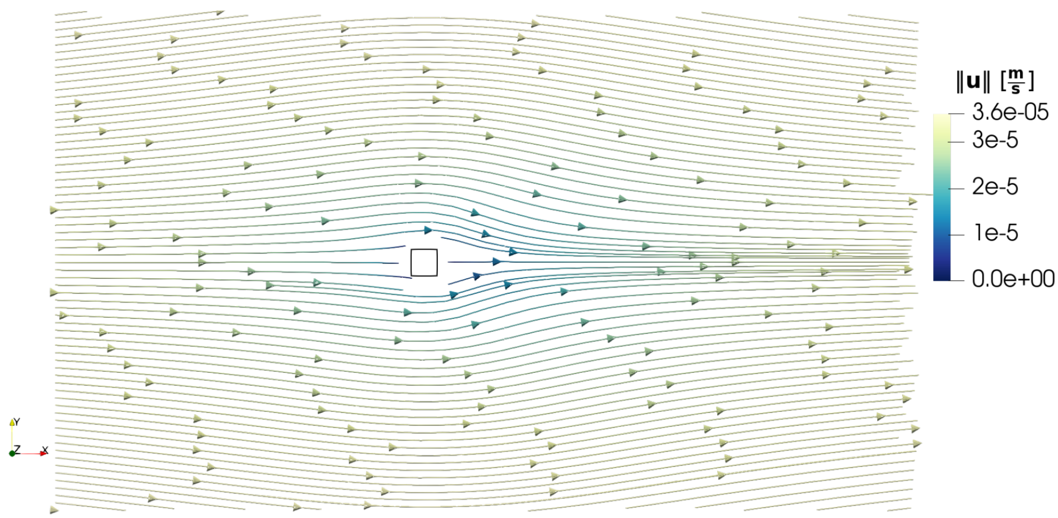

(b)

Figure 28: Absolute velocity streamlines results for $0.1m$ side square vicinity. Simulation: Python/ANSYS, visualization: ParaView. (**a**) ANSYS simulation. (**b**) BEM simulation.

Figures 23-25 show an approximation of laminar flow behavior around a submerged object. Results from ANSYS are considered as a point of comparison. Results obtained with the BEM formulation and singular integral solution (subfigures (b)) presented in section 3 preserve the general order of magnitude of the absolute velocity. The BEM results approximate changes in velocity of the free flow due to the obstruction caused by the submerged objects. This approximation preserves the no-slip boundary condition defined. Nonetheless, some differences in the changes of velocity and overall flow characteristics between the simulations is observed. A bigger region of free flow is affected (fluctuations in direction and magnitude of the free flow) by the submerged objects in the BEM simulations as can be seen in Figures 26-28.

The two main noticeable differences between the results obtained from ANSYS and BEM simulations are the following. (1) A gradient of the velocity with a smaller slope, in comparison to ANSYS, is present in BEM simulation as can be seen in regions marked with B in Figures 23b, 24b and 25b. (2) A wider region of free flow is disturbed around the submerged object and free flow is achieved further from the object (region A in Figures 23b, 24b and 25b) in comparison to the ANSYS simulation.

4.5 Convergence of the Boundary Unknowns

The convergence of the *unknown* boundary conditions ($\mathbf{X}$) in the iterative cycle are given as additional results (see Figure 29). This manuscript does not assess the convergence of the solution as its objective. The objective is to implement a simplified analytic integration scheme to solve the boundary problem. These results aid in assessing whether a stable solution is achieved in the numerical examples. This can be seen with the behavior of the boundary solutions in Figure 29. Random boundary elements where selected to visualize the history of their $\mathbf{X_1}$ boundary conditions for 40 iterations.

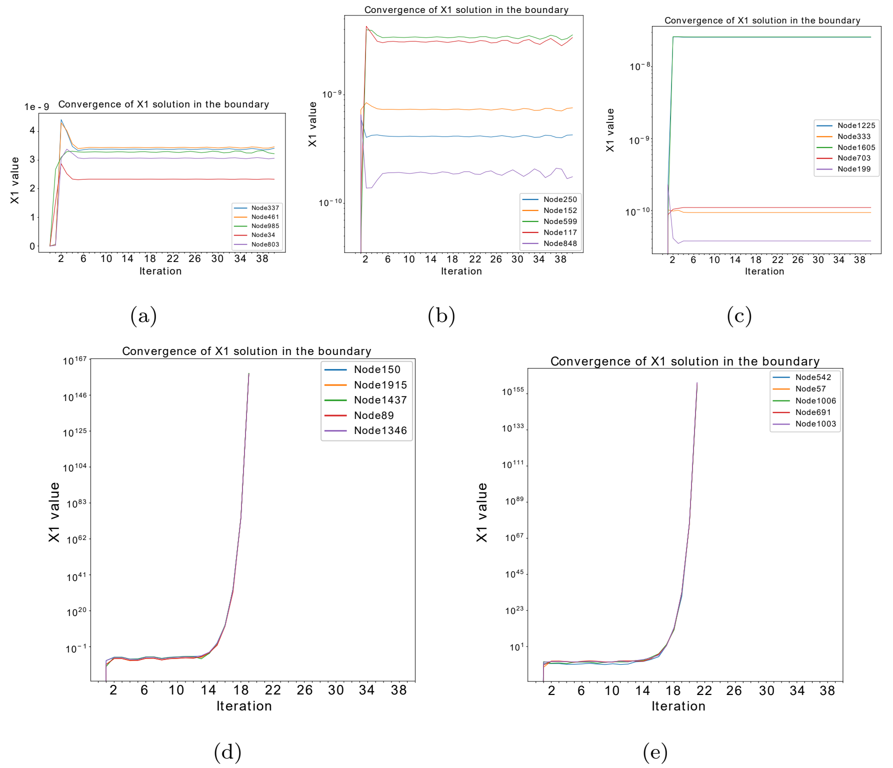

Figure 29: Convergence of unknown values $\mathbf{X}_1$ in B. Random boundary elements (functional node) selected. (**a**) Airfoil at $\mathbf{0}°$ Angle of Attack. (**b**) Airfoil at $\mathbf{3}°$ Angle of Attack. (**c**) Square of 0.1 m side. (**d**) Circle of 0.5 m radius. (**e**) Ellipse of 1 m major axis.

For the cases of the circle and ellipse (Figures 29(d) and 29(e)), an initial intention of convergence (low variation of the results) is achieved for the first 10-14 iterations. After the 14th iteration the divergence is exponential and no boundary solution can be found. This explains why no u_i field is presented for these cases. It can be seen that examples with small geometric changes (circle and ellipse) present an accelerated divergence of the boundary results.

For the airfoil's examples (Figures 29(a) and 29(b)) a stable convergence is achieved for the first 20 iterations. After the 20th iteration the results have a slower tendency of divergence. In contrast, the square example (Figure 29(c)) presents a stable convergence through the 40 iterations. This indicates that examples with strong geometric changes have a tendency of convergence.

5 Conclusions and Future Work

This manuscript presents the simplification and evaluation of a fluid dynamics problem using the Boundary Element Method. The solution of the singular boundary and surface integrals are performed with the source node displacement method and direct analytic evaluation, respectively, as the contribution. To the best of our knowledge, these singularity avoiding methods have not been implemented for the evaluation of such integrals in the specific fluid dynamics field. Thus, it provides a simplified alternative to computing singular integrals. The advantages of the analytic approaches are their precision and low computational costs. In addition, the analytic methods provide insight about the concept of singular integrals in BEM formulation.

As can be seen in sections 4.1 and 4.3, the implemented source node displacement method can approximate the singular boundary integrals. The results of these integrals for Green's function F are exact with the results from [1]. In comparison, there is a discrepancy with the results of Green's function G. However, we are unaware of any semantic that justifies the difference between the null result obtained from [1] and our result. In addition, it can be seen that the result for the singular integral of the Green function G with the source node displacement method is identical to the analytic integral result obtained without avoiding the singularity. As a consequence, it can be said that the boundary integrals are correctly computed for a canonical element with the source node displacement method.

Our implementation predicts laminar flow characteristics around some submerged objects. It retains the order of the magnitude of the free-flow velocity and to some degree approximates the expected flow direction. Differences can be found in the flow region around the submerged objects where convective acceleration occurs. As well as difficulties in the convergence of the boundary conditions for other objects. These differences may occur due to factors not assessed which do not correspond to the goal of this manuscript. Factors such as a not sufficient discretization, the geometry of the submerged objects, and the order of the elements used. Even though these uncertainties arise, the approximations of the singular integrals can be computed by the means presented and are compared by a different method other than the numerical simulation examples. As a consequence, it can be said that the goal of the article is accomplished, in which the singular integrals are computed and tested by means of the presented methods.

Our simulation was developed for free flow cases with constant free flow velocity. Despite this fact, the exposed methodology and solution of singular integrals can be applied to different examples in which, for example, the free flow velocity fluctuates.

Since we do not focus our attention in some aspects of the BEM, there is a possibility for future work to improve the convergence of the boundary solution, extend the integration schemes to higher order elements, assess the necessary interior to be discretized, as well as extend the implemented methods for avoiding the singularities in other scientific fields.

References

[1] Abdel-Magid Abdel-Latif Abdalla. Solution of viscous flow problems by using the boundary element method. 1992.

[2] C Balakrishna, LJ Gray, and JH Kane. Efficient analytical integration

of symmetric galerkin boundary integrals over curved elements; elasticity formulation. *Computer methods in applied mechanics and engineering*, 117(1-2):157–179, 1994.

[3] PK Banerjee and ST Raveendra. New boundary element formulation for 2-d elastoplastic analysis. *Journal of engineering mechanics*, 113(2):252–265, 1987.

[4] Prasanta Kumar Banerjee and Roy Butterfield. *Boundary element methods in engineering science*, volume 17. McGraw-Hill London, 1981.

[5] Prasanta Kumar Banerjee and Luigi Morino. *Boundary Element Methods in Nonlinear Fluid Dynamics: Developments in boundary element methods-6*. CRC Press, 1990.

[6] RGR Camacho and JR Barbosa. The boundary element method applied to incompressible viscous fluid flow. *Journal of the Brazilian Society of Mechanical Sciences and Engineering*, 27(4):456–462, 2005.

[7] Thomas A Cruse. An improved boundary-integral equation method for three dimensional elastic stress analysis. *Computers & Structures*, 4(4):741–754, 1974.

[8] GF Dargush and PK Banerjee. A boundary element method for steady incompressible thermoviscous flow. *International journal for numerical methods in engineering*, 31(8):1605–1626, 1991.

[9] Xiao-Wei Gao. A promising boundary element formulation for three-dimensional viscous flow. *International journal for numerical methods in fluids*, 47(1):19–43, 2005.

[10] Xiao-Wei Gao. An effective method for numerical evaluation of general 2d and 3d high order singular boundary integrals. *Computer methods in applied mechanics and engineering*, 199(45-48):2856–2864, 2010.

[11] Xiao-Wei Gao, Jin-Bo Zhang, Bao-Jing Zheng, and Ch Zhang. Element-subdivision method for evaluation of singular integrals over narrow strip boundary elements of super thin and slender structures. *Engineering Analysis with Boundary Elements*, 66:145–154, 2016.

[12] LJ Gray, Luiz F Martha, and AR Ingraffea. Hypersingular integrals in boundary element fracture analysis. *International journal for numerical methods in engineering*, 29(6):1135–1158, 1990.

[13] JC Lachat and JO Watson. Effective numerical treatment of boundary integral equations: a formulation for three-dimensional elastostatics. *International Journal for Numerical Methods in Engineering*, 10(5):991–1005, 1976.

[14] Hans Petter Langtangen and Geir K Pedersen. *Scaling of differential equations*. Springer International Publishing Berlin, Germany:, 2016.

[15] YJ Liu. On the simple-solution method and non-singular nature of the bie/bem-a review and some new results. *Engineering analysis with boundary elements*, 24(10):789–795, 2000.

[16] Aaron Meurer, Christopher P. Smith, Mateusz Paprocki, Ondřej Čertík, Sergey B. Kirpichev, Matthew Rocklin, AMiT Kumar, Sergiu Ivanov, Jason K. Moore, Sartaj Singh, Thilina Rathnayake, Sean Vig, Brian E. Granger, Richard P. Muller, Francesco Bonazzi, Harsh Gupta, Shivam Vats, Fredrik Johansson, Fabian Pedregosa, Matthew J. Curry, Andy R. Terrel, Štěpán Roučka, Ashutosh Saboo, Isuru Fernando, Sumith Kulal, Robert Cimrman, and Anthony Scopatz. Sympy: symbolic computing in python. *PeerJ Computer Science*, 3:e103, January 2017.

[17] Hai-Feng Peng, Miao Cui, and Xiao-Wei Gao. A boundary element method without internal cells for solving viscous flow problems. *Engineering Analysis with Boundary Elements*, 37(2):293–300, 2013.

[18] JJ Pérez-Gavilán. Introducción a los elementos de frontera. *México, Consejo Nacional de Ciencia y Tecnologıa*, 2006.

[19] Elias M Stein. *Singular integrals and differentiability properties of functions*, volume 2. Princeton university press, 1970.

[20] JCF Telles. A self-adaptive co-ordinate transformation for efficient numerical evaluation of general boundary element integrals. *International journal for numerical methods in engineering*, 24(5):959–973, 1987.

[21] Guizhong Xie, Yudong Zhong, Fenglin Zhou, Wenliao Du, Hao Li, and Dehai Zhang. Singularity cancellation method for time-domain boundary element formulation of elastodynamics: A direct approach. *Applied Mathematical Modelling*, 80:647–667, 2020.

[22] Li Yuan, Mao Wentao, Wang Gangsheng, Liu Jing, and Wang Shixun. A general-purpose machine learning framework for predicting singular integrals in boundary element method. *Engineering Analysis with Boundary Elements*, 117:41–56, 2020.